(Received 25 February 2025, Accepted 11 April 2025, Scheduled 29 April 2025)

Comparative Assessment of Two Numerical Methods for Eddy Current Nondestructive Evaluation: Insights from Benchmark Studies

Rebeka Sultana[1,2], Mingyang Lu[2], Yuan Ji[3], John C. Aldrin[4], and Jiming Song[1,2,*]

[1]*Department of Electrical and Computer Engineering, Iowa State University, Ames, IA 50011, USA*
[2]*Center for Nondestructive Evaluation (CNDE), Iowa State University, Ames, IA 50011, USA*
[3]*Department of Applied Engineering Technology, Virginia State University, Petersburg, VA 23806, USA*
[4]*Computational Tools, Gurnee, IL 60031, USA*

ABSTRACT: Numerical modeling of eddy current (EC) phenomena is pivotal in nondestructive evaluation (NDE). It has become invaluable in NDE industries, contributing to probe design, inspection procedures, defect characterization, model training, and results interpretation. This study comprehensively explores two numerical methods — Volume Integral Method (VIM) and Finite Element Method (FEM) to assess their suitability for EC NDE. Four test cases involving varying geometries, defect types, and probe configurations were modeled to compare computational compatibility. Numerical results are evaluated for their accuracy, efficiency, and practical implications. Results indicate a reasonable correlation between the two methods, with VIM excelling at computational efficiency for simpler geometries, and FEM demonstrating robustness for complex configurations. The findings highlight the strengths and limitations of each method, aiding users in selecting appropriate techniques for defect characterization and optimizing inspection conditions.

1. INTRODUCTION

Eddy current (EC), an outcome of electromagnetic induction phenomena [1], is a prominent nondestructive evaluation (NDE) technique valued for its high sensitivity, precision, and noncontact nature for inspecting metallic composites. Its ability to penetrate coating layers makes it indispensable in several industries [2–4] such as steel, aerospace, metallurgy, rail transport, and energy generation. Despite variations in EC instrumentation to meet different testing needs, their working principles remain consistent. A driver coil (source) with an alternate current (AC) is often positioned close to the conductive specimen. According to Maxwell's induction law [1], AC generates a magnetic field that interacts with the specimen and induces eddy currents. Defects or anomalies, such as corrosion or cracks inheriting different electrical properties than the host specimen, disrupt the EC flow and alter the magnetic field distribution [5, 6]. The disturbance in induced EC magnitude and phase can be detected by measuring the signal variations in the primary driver or secondary receiver coil. The accuracy of the detections largely depends on the design and selection of EC probes' sensitivity to the magnetic field distribution, which is directly influenced by the shape and geometric characteristics of the detection coil [7, 8]. For example, small, high-frequency probes offer excellent spatial resolution but limited penetration, while larger, low-frequency probes provide deeper penetration at the expense of resolution. Therefore, a single EC absolute probe cannot satisfy all requirements in detection tasks. This diversity in requirements necessitates a variety of probe designs [9–11] from reflection differential probes to encircling bobbins for specific applications. In this context, numerical modeling emerges as an indispensable tool, enabling engineers to optimize probe designs and simulate diverse test scenarios before on-site implementation, thus reducing the dependency on costly trial-and-error processes.

The fundamental objective of nondestructive testing (NDT) is to maintain the integrity of the structures throughout the manufacturing procedures. Numerical modeling can contribute significantly at different process stages [12, 13] to assist in achieving this goal, as it provides a cost-effective and reliable means to simulate and optimize various aspects of inspection and design. Over the years, numerical modeling methods based on different discretization techniques [14, 15] have been developed including the finite element method (FEM) [16], finite volume method (FVM) [17], finite integration technique (FIT) [18], volume integral method (VIM) [19], and many others. Verifying whether the numerical methods align with experimental results is crucial before deciding on credential usage. However, selecting the most appropriate numerical method remains a challenge, especially when experimental validation data are unavailable. In such cases, comparing multiple numerical modeling methods offers an alternative for assessing reliability.

This study aims to evaluate the reliability and efficiency of two numerical methods, VIM and FEM, for solving EC defect detection problems across a variety of test scenarios. The VIM approach solves the integral forms of electromagnetic formulations, while the FEM approach solves partial differential

* Corresponding author: Jiming Song (jisong@iastate.edu).

forms. This work presents four test cases derived from earlier research works, which have been solved using a single numerical method, noting the unavailability of experimental data for repeatability. Unlike previous studies focusing on introducing novel techniques by correlating a single numerical approach with experimentation, this work emphasizes a comparative evaluation of two numerical methods to provide practical insights into selecting the most suitable one. This research assesses the strengths and weaknesses of VIM and FEM, focusing on computational efficiency and accuracy in capturing defect responses for different EC inspection scenarios. The organization of this work is followed by overviewing the numerical methods in Section 2, modeling and analysis of computational results in Section 3, and the conclusions of the study in the last section.

2. NUMERICAL METHODS OVERVIEW

The EC problem is an electromagnetic problem which involves solving either partial differential equations (PDE) or integral equations. Since the two methods evaluated in this study are based on two different mathematical approaches, the formulation and accounting of boundary conditions are briefly discussed before presenting the modeling and numerical results. The foundation of VIM is the derivation of an integral form [20] of the EC problem domain that accounts for the electromagnetic induction phenomenon. The integral computation of electric or magnetic field response using Green's function is given in Equations (1) and (2). $\mathbf{E}^{(i)}$ is the incident electric field at the defect due to the source coil in free space; $\mathbf{J}$ represents the unknown current due to the defect in the host medium, which is in the testpiece; and $\mathbf{E}$ is the total field in the testpiece with presence of the defect. The integral equations [20, 21] are solved using Green's function ($\overline{\mathbf{G}}(\mathbf{r}, \mathbf{r}')$), which depends on the distance between the source and field points. In this method, the field at a specific point is calculated by summing the effects of sources at all points.

$$\mathbf{E}(\mathbf{r}) + j\omega\mu \iiint_{V_f} \overline{\mathbf{G}}(\mathbf{r}, \mathbf{r}') \cdot \mathbf{J}(\mathbf{r}')\, dv' = \mathbf{E}^{(i)}(\mathbf{r}) \quad (1)$$

$$\mathbf{J}(\mathbf{r}') = (\sigma(\mathbf{r}') - \sigma_h)\, \mathbf{E}(\mathbf{r}') \quad (2)$$

where ω = angular frequency, μ = testpiece permeability, V_f = defect region, and σ_h = testpiece conductivity, $\sigma(\mathbf{r}') = \sigma_h$ or 0 when $\mathbf{r}'$ is in the testpiece or in defect region respectively.

VIM solves the unknowns for a compact source domain by discretizing the anomalous region with the regular volumetric grid. By applying Galerkin's method of moments [21] discretization technique, the Equation (1) can be derived for each discretized element in Equation (3).

$$\delta_z \mathbf{I}_{lmq} + \sigma_{lmq} \sum_{Q=0}^{N_z} \sum_{L=0}^{N_x} \sum_{M=0}^{N_y} \mathbf{G}_{qQ}(l-L, m-M) \cdot \mathbf{I}_{LMQ} = \mathbf{I}_{lmq}^{(i)} \quad (3)$$

$\mathbf{I}_{lmq}^{(i)}$ is the incident current density in the defect region, and σ_{lmq} is the electrical conductivity of the defect, where l, m, and q are the indexes for the corresponding discretized volume grid. $\mathbf{I}_{LMQ}$ is the basis function, and matrix $\mathbf{G}_{qQ}$ is the Fourier transform of Green's function that accounts for the field distribution along x- and y-axes. δ_z represents the discretization depth along the z-axis. N_x, N_y, and N_z represent the number of meshes or discretized elements along the x-, y-, and z-axes. Once the electric field or equivalent current is solved in the defect region, the electric and magnetic fields are calculated to find the induced current or voltage in the coil and the magnetization in the presence of a magnetic core.

The VIM is efficient because it requires the modeling of unknown electric currents and magnetic sources, which is for defective regions only. However, the integral equation is not well defined for all the arbitrary shapes that a probe or a defect may have in practical eddy current problems. In contrast, the FEM's ability to discretize a nonhomogeneous region into numerous sub-regions allows the method to model a wide variety of probe and defect geometries. The PDE used [22] in modeling EC problems can be derived in terms of magnetic vector ($\mathbf{A}$) and electric scalar (Φ) potentials, and source current density ($\mathbf{J}_s$) in Equations (4) and (5). σ is the electrical conductivity of the host medium.

$$\nabla \times \mu^{-1} \nabla \times \mathbf{A} + j\omega\sigma\mathbf{A} + \sigma\nabla\Phi = \mathbf{J}_s \quad (4)$$

$$\nabla \cdot (j\omega\sigma\mathbf{A} + \sigma\nabla\Phi) = 0 \quad (5)$$

$\mathbf{A}$ is the total magnetic potential due to the source potential ($\mathbf{A}_s$) in free space. By applying the Galerkin method in Equations (4) and (5), the FEM formulation [22, 23] can be approximated by Equations (6) and (7).

$$\int_{V_c} \nabla \times \mathbf{N}_i \cdot \mu^{-1} \nabla \times \mathbf{A}^{(n)}\, dv + \int_{V_c} j\omega\sigma \mathbf{N}_i \cdot \mathbf{A}^{(n)} dv + \int_{V_c} \sigma \mathbf{N}_i \cdot \nabla\Phi^{(n)} dv = \int_{V_c} \nabla \times \mathbf{N}_i \cdot \mu_0^{-1} \nabla \times \mathbf{A}_s dv, \quad i = 1, 2, ..., 6 \quad (6)$$

$$\int_{V_c} j\omega\sigma \nabla L_i \cdot \mathbf{A}^{(n)} dv + \int_{V_c} \sigma \nabla L_i \cdot \nabla\Phi^{(n)} dv = 0, \quad i = 1, 2, ..., 4 \quad (7)$$

In the above equations, $\mathbf{N}_i$ and $\mathbf{L}_i$ denote the basis functions for the ith edge and ith node respectively for the nth element. $\mathbf{A}^{(n)}$ is the induced magnetic vector potential, and $\Phi^{(n)}$ is the electric scalar potential in element n. V_c represents the volume of the conductive testpiece. The electric field can be calculated once the magnetic vector potential and electric scalar potential are obtained with the following relation of $\mathbf{E} = -j\omega\mathbf{A} - \nabla\Phi$. In FEM, since the EM fields are calculated in a finite region by approximating the fields at the boundary, the perfect electric conductor boundary condition is one of the approximations of the exterior finite boundary.

3. MODEL BENCHMARK TEST CASES STUDIES

In our earlier work [24], we modeled some well-known EC benchmark cases with applying VIM and FEM that presented

TABLE 1. Problem specification for Test Case 1.

Coil Specification	Values	Sample & Defect Specification	Values
Outer radius (a_1)	12.4 mm	Sample thickness (t)	12.22 mm
Inner radius (a_2)	6.15 mm	Sample conductivity (σ)	30.6 MS/m
Coil height (h)	6.15 mm	Defect length (l)	12.6 mm
Turns	3790	Defect depth (d)	5.0 mm
Frequency	900 Hz	Defect width (w)	0.28 mm
Lift-off	0.88 mm	Coil separation (s)	30 mm

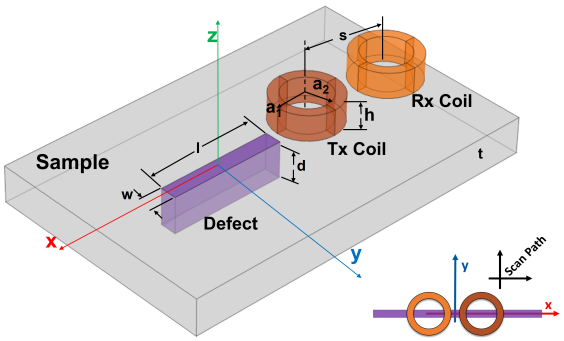

FIGURE 1. Schematic for a rectangular testpiece with a rectangular notch and reflection surface probe (Tx-Rx coils, Case 1).

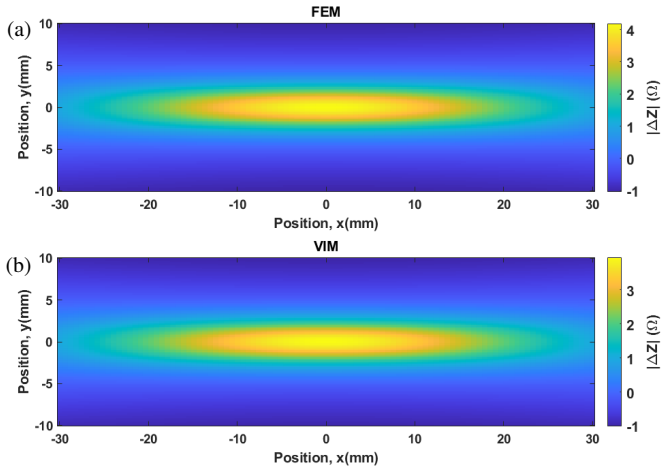

FIGURE 2. 2D surface plot of absolute impedance change (ΔZ) in ohms for (a) FEM and (b) VIM as a function of the probe's center position in the x-y plane. The midpoint between Tx and Rx is considered as probe center. The defect's center is at the origin of the x-y plane.

good agreements with measurement data. However, those benchmark cases were limited to rectangular testpieces with a single absolute coil. This study extends the scope to more diverse scenarios, incorporating variations in testpiece shapes, defect geometries, and probe types. The test cases include rectangular and cylindrical testpiece samples with probes ranging from reflection surface to differential encircling and array configuration. In this work, we use two commercial software tools — VIC-3D [25] and COMSOL [26] for implementing VIM and FEM, respectively.

The numerical modeling begins with discretizing (meshing) the electromagnetic problem domain into small elements and solving the equations for electric and magnetic field distributions. For EC problems, the skin depth (δ), which dictates the penetration of the EC signal [1], plays a critical role in determining the required number of mesh elements for adequately discretizing the sample and defect domains. δ can be calculated as $\sqrt{2/(\omega\mu\sigma)}$, which depends on the electrical conductivity, magnetic permeability of the test specimen, and operating frequency of the probe. From prior knowledge of convergence study for efficient meshing, we maintained a minimum of 5–7 mesh elements per skin depth along defect depth. Since the wavelength in the metal is 2π times of the skin depth, 5–7 mesh elements per skin depth is reasonable to capture the signal penetration responses accurately. For FEM model, to model a large free space, the truncation boundary was kept 6–8 times of the coil's larger dimension. In both modeling techniques, the defect center is considered the origin of the coordinate system, and a probe scan has been performed over the defect area. For analyzing the results, the impedance changes (ΔZ) were computed as the difference between defective and defect-free conditions.

3.1. Test Case 1: Transmitting Receiving Coil Configuration for Notch in a Rectangular Plate

The problem specification presented in Fig. 1 is derived from [27]. The original problem is with a single absolute coil, whereas here, an additional receiver coil is considered in the problem scenario. The receiver coil has the same dimensions as the driver coil. The distance (s) between the axis of the two coils is 30 mm. The test case consists of a conductive plate (σ = 30.6 MS/m, 12.6 mm thick) with a rectangular notch above which the probe moves. The transmitter-receiver (Tx-Rx) type probe works in the reflection mode; the transmitter coil induces the EC in the conductive sample, and the receiver coil picks up the signal from the sample. The specifications for the problem are provided in Table 1.

The excitation frequency is 900 Hz. At this testing frequency, δ is 3.04 mm, where the depth of the defect is almost 2δ. A proper dense mesh is employed in the defect domain to increase the modeling accuracy. In Table 2, the mesh elements used for two methods have been given. In FEM, free tetrahedral mesh elements are used for defect modeling. The maxi-

TABLE 2. Number of mesh elements for Test Case 1.

VIM	FEM		
Defect Domain ($N_x \times N_y \times N_z$)	Coil Domain (Tetrahedral)	Defect Domain (Tetrahedral)	Total Elements
$64 \times 2 \times 16 \sim 2\,\text{k}$	Tx + Rx: 3 k + 3 k (max size: 7.7 mm)	10 k (max size: 0.25 mm)	153 k

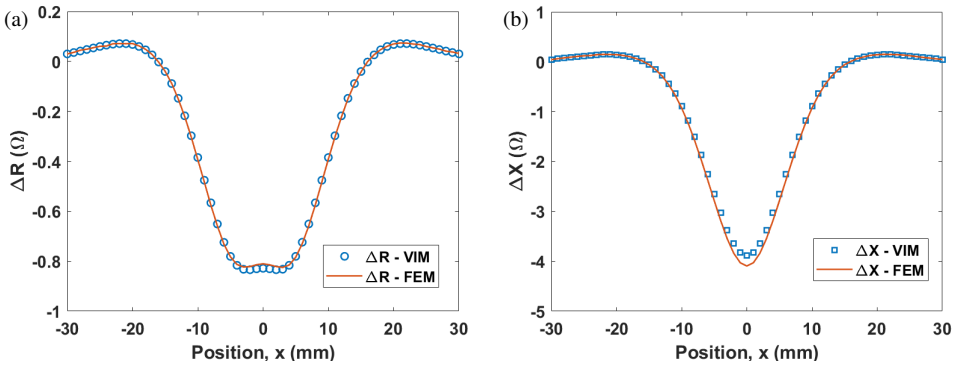

FIGURE 3. (a) Real part (ΔR) and (b) imaginary part (ΔX) of impedance change (ΔZ) as a function of the probe's center position (x) along the x-axis. The midpoint between Tx and Rx is considered as probe center.

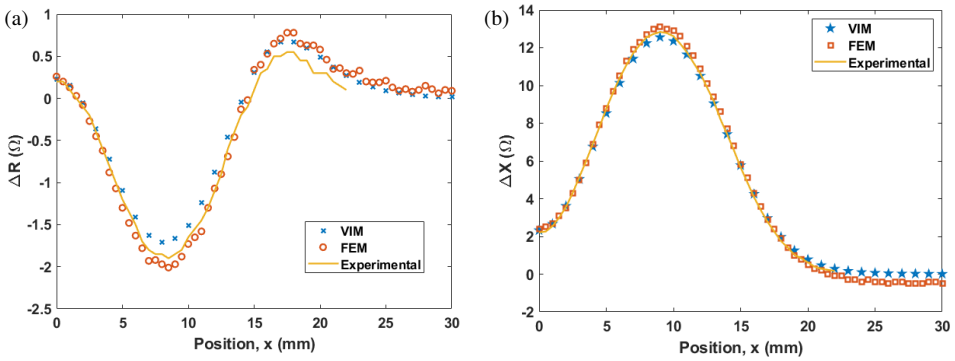

FIGURE 4. (a) Real part (ΔR) and (b) imaginary part (ΔX) of impedance change (ΔZ) as a function of the probe's (single absolute coil) center position (x) along the x-axis.

mum (max) size is kept at 0.25 mm to have at least 2 elements along the defect width which is 0.28 mm. This max size is the maximum edge dimension of the tetrahedral mesh that generates around 10,000 elements in the volume defect domain. In VIM, the defect domain is discretized with hexahedral voxel grids by assigning the number of mesh elements 64, 2, and 16 along the defect length, width, and depth, respectively, which is around 2,000 elements for the defect volume. The number of unknowns solved by VIM for 2,000 mesh elements is 5,000. There are three unknowns for each internal discretized element and only one or two for the boundary element.

A C scan is performed over the defect area with a 1 mm step along the x-direction of ± 30 mm range and along the y-direction for ± 10 mm range. The raster scans of impedance data from two methods are plotted in a 2D graph shown in Fig. 2. A slight variation in the absolute value of impedance change can be observed from the 2D color bar magnitude scale. For more insightful comparison purposes, in Fig. 3, the impedance change response is plotted by scanning along the direction of the defect's maximum length (along the x-axis), considering the probe's position being unchanged along the y-axis. The impedance changes for the real and imaginary parts exhibit excellent agreement from Fig. 3. The results demonstrate that the receiver coil's responses calculated by both methods are very similar. The root mean square error (RMSE) is calculated at 0.006 Ω for the real part and 0.083 Ω for the imaginary part. Since the experimental data for Test Case 1 is unavailable, a comparison is drawn between the two methods. Nonetheless, as presented in Fig. 4, a good agreement is achieved between simulations and experiments [27] where all the parameters were as exact as for this test case, except that the probe was a single absolute coil. The RMSE with respect to the measurement data is 0.189 Ω (real part) and 0.149 Ω (imaginary part) for VIM calculation, and 0.191 Ω (real part) and 0.145 Ω (imaginary part)

TABLE 3. Problem specification for Test Case 2.

Coil Specification	Values	Sample & Defect Specification	Values
Outer radius (a_1)	5 mm	Sample inner diameter	10 mm
Inner radius (a_2)	3 mm	Wall thickness (t)	5 mm
Coil height (h)	2 mm	Sample Conductivity (σ)	1.02 MS/m
Turns	200	Defect diameter ($2r$)	1.0 mm
Frequency	1 kHz	Defect depth (d)	2.5 mm

TABLE 4. Number of mesh elements for Test Case 2.

VIM	FEM		
Defect Domain ($N_x \times N_y \times N_z$)	Coil Domain (Tetrahedral)	Defect Domain (Tetrahedral)	Total Elements
$8 \times 8 \times 8 \sim 0.5$ k	2.8 k (max size: 0.8 mm)	1 k (max size: 0.27 mm)	110 k

for FEM. Following the agreement between measured data and numerical results from Fig. 4 with an absolute coil, it provides confidence in predicting reasonable results for the transmitter-receiver (driver-pickup) probe by both numerical methods if compared with real measurement.

3.2. Test Case 2: Single Coil Configuration in a Pipe with a Flat-bottom Hole

For the second test case, a configuration with cylindrical geometry is modeled to replicate the pipeline inspection's test environment. The model geometry consists of a tube, a coil, and a defect. An absolute type of bobbin coil (the coil axis is parallel to the tube axis) is used for calculating the signal change. The tube wall is 5 mm thick stainless steel with a conductivity of 1.02 MS/m. The defect geometry is a cylindrical hole, known as a flat-bottom hole (FBH). The FBH is surface breaking on the inner side of the tube through to half of the pipe wall with a 1 mm diameter. The skin depth is 15.76 mm at 1 kHz which penetrates through the tube's outer wall. Since the defect is on the inner side, a bobbin coil is used to scan the inside of the steel pipe along the pipe's axial direction. The schematic representation is depicted in Fig. 5, and the parameters for the problem description are provided in Table 3. Meshing with FEM is always

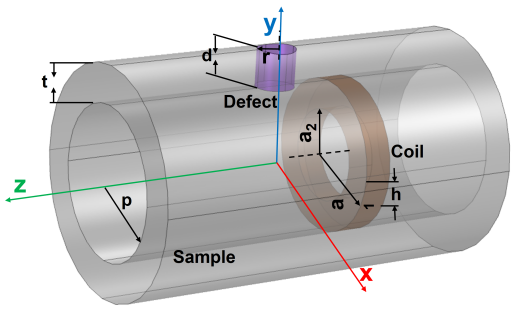

FIGURE 5. Schematic for a cylindrical test piece with an inner surface breaking FBH and an absolute bobbin coil (Case 2).

a meticulous task when the geometry comprises many domains and boundary layers. For example, in Test Case 2, the adjacent flat surface of FBH and the inner curved face of the pipe wall create a very thin gap, as depicted in Fig. 6. The best practice is to discretize these connected thin surfaces using edge elements and boundary elements type mesh to distinguish the defect and host medium. An approximate number of mesh elements is tabulated in Table 4 to indicate the mesh density used for solving the problem. With VIM, the sample test piece does not need to be discretized; only the small defect domain, which interrupts the EC flow, needs to be meshed.

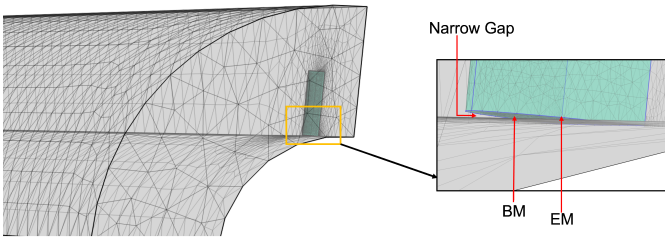

FIGURE 6. FEM meshing for narrow region, where BM indicates boundary mesh elements, and EM indicates edge mesh elements.

Inside the pipe, a B scan is performed for a range of ± 10 mm with a 1 mm step along the z-direction, keeping the FBH centered at the coordinate origin. The numerical results for impedance change are plotted in Fig. 7, which indicates an excellent agreement between the two methods. The RMSE for the real part is 1.25 μΩ and 0.352 μΩ for the imaginary part, where the range of impedance change is approximately 135 μΩ and 13 μΩ, respectively. Since there is no measurement data, we looked into finding a similar test scenario in cylindrical coordinates with reference data, which can be comparable to the performance of the numerical findings. In [28], the authors worked with a cylindrical test piece, where the coil axis is perpendicular to the tube sample's axis (pancake coil), and the flaw is

TABLE 5. Problem specification for Test Case 3.

Transmitter Coil (Tx)	Values	Receiver Coil (Rx)	Values	Sample & Defect Specification	Values
Inner diameter	47 mm	Inside diameter	41 mm	Inner diameter ($2p$)	16 mm
Width (w_1)	2.4 mm	Width (w_2)	1 mm	Wall thickness (t)	8 mm
Height (h_1)	30 mm	Height	2 mm	Sample Conductivity (σ)	1.43 MS/m
Turns	200	Turns	200	Defect diameter ($2r$)	3.5 mm
Frequency	3 kHz	Rxs' separation (s)	2 mm	Defect depth (d)	3 mm, 5 mm

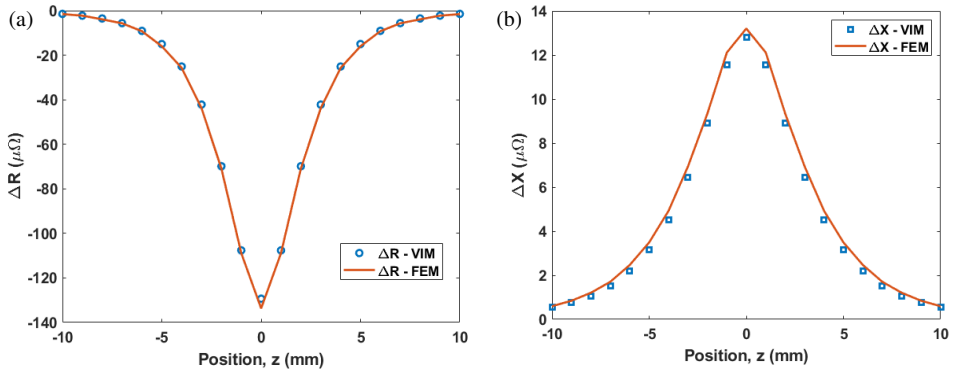

FIGURE 7. (a) Real part (ΔR) and (b) imaginary part (ΔX) of impedance change (ΔZ) as a function of the coil's center position (z) along the z-axis. The defect's base is centered in the x-z plane.

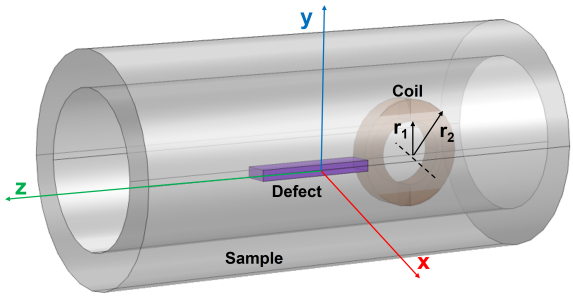

FIGURE 8. Schematic for a cylindrical test piece with a rectangular notch and a rotary pancake coil.

a rectangular notch. The reference test model is presented in Fig. 8. It is worth noting that the tool we used for VIM has well-established integral formulation for modeling transformed coil geometry (pancake coil, tangent coil, tilted coil) in a rectangular (planar) coordinate system efficiently. However, such formulation for transformed coil domain in cylindrical coordinates has not been employed yet. Nonetheless, we modeled the problem with FEM alone and compared the result with the measured data [28] for 25 kHz, as plotted in Fig. 9. It is discernible from Fig. 9 that the FEM approach reproduces the reference data acceptably. By correlating Figs. 8 and 9, it is assumable that both methods can solve simple cases in cylindrical coordinates with reasonable numerical calculations. If such test inspection as in Test Case 2 requires investigation for practical implications or model-assisted probability of detection (MAPOD) data generation, VIM can be an efficient choice because of fewer computational requirements.

3.3. Test Case 3: Differential Encircling Coil Configuration for a Pipe with Varying Flat-Bottom Hole Size

Test Case 2 models a problem specification for the cylindrical workpiece with a simple absolute coil. Following that, for Test Case 3, a complex but frequently used differential encircling probe is designed. The differential encircling probe has the advantage of detecting small subsurface flaws. In this problem setup, the probe configuration comprises two receiver coils (Rxs) working in differential mode and a driver coil encircling the Rxs. In this test case, the test specimen is a stainless-steel pipeline ($\sigma = 1.43$ MS/m) with inner and outer diameters of 16 mm and 32 mm, respectively. The test specification is drawn in Fig. 10. In the actual test setup for Benchmark #6 in [29], the test piece houses three different sizes of FBH and a groove. In our study, we modeled two FBH defects that buried 37.5% (FBH 3) and 62.5% (FBH 5) from the outer surface of the pipe wall, where the thickness of the pipe wall is 8 mm. Table 5 contains the detailed specifications for the problem. In VIM, the differential mode is imposed by setting the direction of the current clockwise (current scaling factor $+1$) for one receiver coil and anticlockwise (current scaling factor -1) for another. In FEM, the receiver coils' current is set to zero, implying an open loop condition. The difference of induced voltages in two open loop coils has been post-processed for impedance calculation. The FBH defects of heights 3 mm and 5 mm fall within 1δ as at 3 kHz operating frequency, the skin depth is 7.7 mm. The number of mesh elements used for different geometric parts is presented in the following Table 6.

TABLE 6. Number of mesh elements for Test Case 3.

VIM	FEM		
Defect Domain ($N_x \times N_y \times N_z$)	Coil Domain (Tetrahedral)	Defect Domain (Tetrahedral)	Total Elements
$8 \times 16 \times 8 \sim 1$ k	Tx: 8.4 k (max size: 0.8 mm) Rxs: 4 k + 4 k (max size: 0.8 mm)	2.1 k (max size: 0.7 mm)	235 k

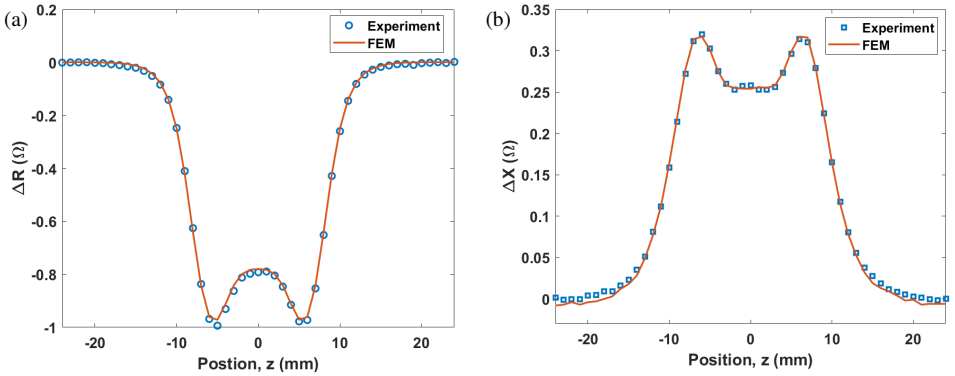

FIGURE 9. (a) Real part (ΔR) and (b) imaginary part (ΔX) of impedance change (ΔZ) as a function of the coil's center position (z) along z-axis.

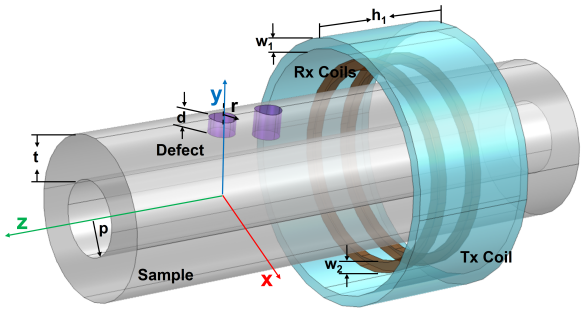

FIGURE 10. Schematic for a cylindrical test piece with outer surface breaking FBHs and an encircling differential probe (Tx-'Rx-Rx') (Case 3). The Tx coil's mid-height ($h_1/2$) point is aligned with the midpoint of the Rxs' separation gap.

The results presented in Fig. 11 show a significant difference in magnitude for both real and imaginary parts obtained by the two methods. The numerical calculation obtained by VIM is almost twice of that of the FEM. The discrepancy is probably attributed to the Rx coil's current scaling factor in the VIM code, which appears incompatible with induced voltage calculations using the FEM for differential mode. However, it is observed that the graphs from the two numerical results have similar trends in shape, and the maximum changes detected by the differential probe are in the same probe position relative to the defect location. The differences in the results are not uncommon occurrences when comparing two different numerical approaches. In [29], only a single data point for different defect sizes was reported without providing detailed information regarding measuring and calibration methods. Though experimental data is the ideal reference for validating the results, in our study, normalization is performed on the numerical data sets to find correlations between these two methods. The normalization factor was defined as the maximum value of the absolute impedance change of the corresponding numerical data sets. As plotted in Fig. 12, the normalized plots exhibit a better correlation for both defect sizes than Fig. 11. Moreover, a close inspection of the normalized plots exhibits noticeable differences between the peak magnitudes of the two defects. For FBH 5 (5 mm depth), the normalized real peak is significantly larger than FBH 3 (3 mm depth). Similarly, a distinguishable difference between the two defects is observable for the normalized imaginary peak. This difference in the normalized peaks can be a considerable reference for indicating different defect sizes by both methods.

Although normalization provides clearer differentiation between defect sizes, it is essential to evaluate the reliability of the unnormalized numerical results. To validate the accuracy of the computed solutions, we employed an additional low-frequency electromagnetic simulation tool, CST Studio Suite [30], as an independent reference. The new benchmark result, labeled as "Ref" in Fig. 13, demonstrates excellent agreement with the FEM solution in both magnitude and trend. This consistency confirms the accuracy and reliability of the FEM results previously presented in Fig. 11. Furthermore, as supported by prior study [24], the FEM approach has been extensively validated and thus can be considered the most acceptable reference among the compared methods.

3.4. Test Case 4: Transmitter Receiver Array Configuration for a Rectangular Defect in a Plate

In the last attempted test case, we investigated the response of an array probe to detect a rectangular subsurface defect in an aluminum slab plate. The test configuration shown in Fig. 14 was taken from [31] and modeled using both numerical meth-

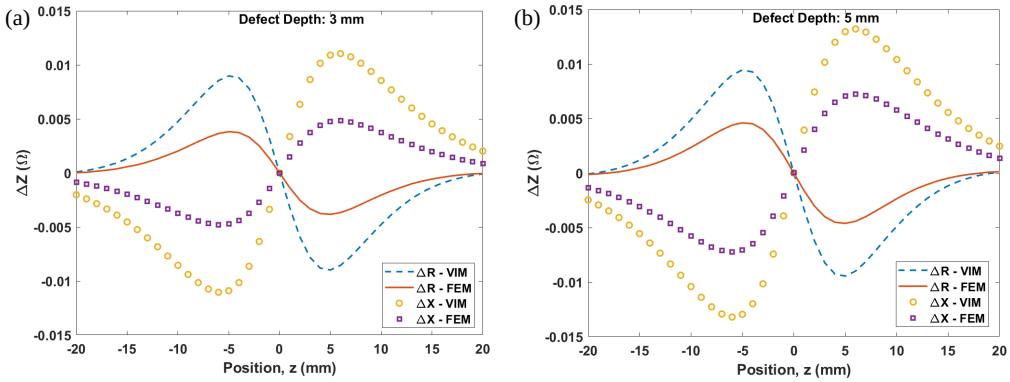

FIGURE 11. Real part (ΔR) and imaginary part (ΔX) of impedance change (ΔZ) as a function of the probe's center position (z) along the z-axis for (a) FBH 3, (b) FBH 5. The defect's base is centered in the x-z plane.

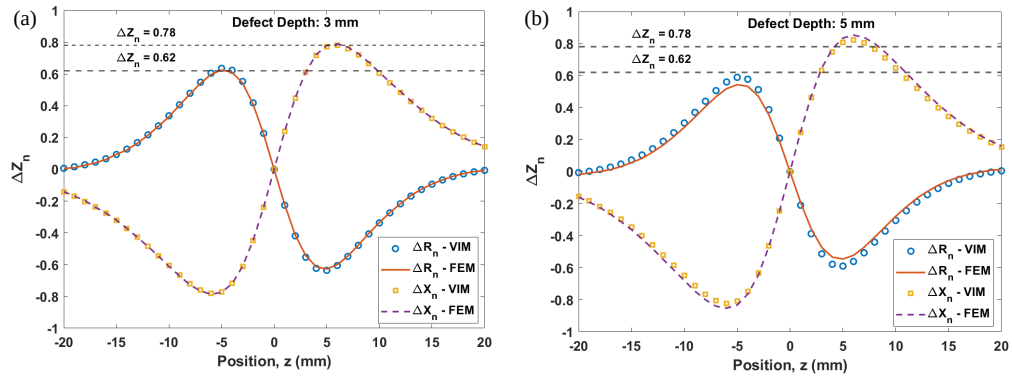

FIGURE 12. Normalized real (ΔR_n) and imaginary part (ΔX_n) of impedance change (ΔZ_n) as a function of the probe's center position (z) along the z-axis for (a) FBH 3, (b) FBH 5. The normalized $\Delta Z_n = \Delta Z / \max|\Delta Z|$.

TABLE 7. Problem specification for Test Case 4.

Coil Tx & Rx	Values	Sample & Defect Specification	Values
Outer radius	10 mm	Sample thickness	10 mm
Inner radius	5 mm	Sample conductivity (σ)	16.4 MS/m
Coil height	10 mm	Defect length (l)	20 mm
Turns	1000	Defect width (w)	20 mm
Frequency	200 Hz	Defect depth (d)	5 mm
Lift-off	2 mm	Coil separation (s)	25 mm

ods. In Test Case 4, the array comprises nine elements arranged in a square pattern. The four receiver coils (Rxs) are placed between the five driver (transmitter) coils (Txs), where one Tx coil is in the middle, and four others are in the corner. The Tx and Rx coils have the exact dimensions. The separation distance (s) from one coil to the adjacent coil is 25 mm (center to center) in both horizontal and vertical directions. The test piece is a 10 mm thick aluminum plate, with the conductivity of 16.4 MS/m, housing a defect with a dimension 20 mm $\times$ 20 mm $\times$ 5 mm. The details are provided in Table 7. Unlike previous test cases with narrow defect width, in this test case, the defect has a significantly large volumetric area. The

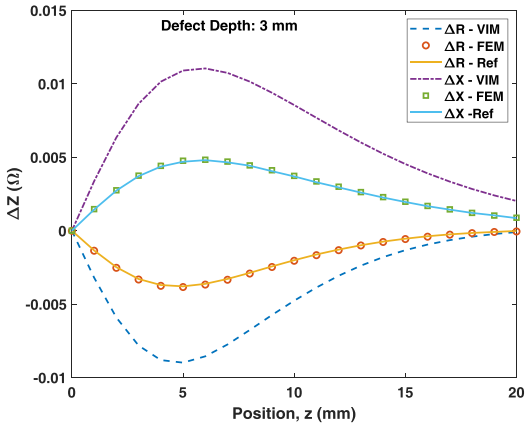

FIGURE 13. Real part (ΔR) and imaginary part (ΔX) of impedance change (ΔZ) as a function of the probe's center position (z) along the z-axis for FBH 3.

array probe is well-suited for covering large inspection areas in less time to accumulate the profile of the defect. The individual probe of the array is 20 mm in diameter with 1,000 turns. The array probe is an electrically large problem to model using both methods. In earlier test cases, the probe domain had one single source, so only a single source point was accountable for calculating the impedance change due to the defect scattered field with VIM. In Test Case 4, with multiple current sources, the

TABLE 8. Number of mesh elements for Test Case 4.

VIM		FEM		
Coil Domain ($N_x \times N_y \times N_z$)	Defect Domain ($N_x \times N_y \times N_z$)	Coil Domain (Tetrahedral)	Defect Domain (Tetrahedral)	Total Elements
$32 \times 32 \times 16 \sim 16\,\text{k}$	$8 \times 16 \times 8 \sim 1\,\text{k}$	Txs & Rxs: 105 k (max size: 3.3 mm)	4.2 k (max size: 0.7 mm)	450 k

TABLE 9. Computational requirement by the numerical methods.

Test Case	Scanning Points	VIM				FEM		
		No. of Mesh Elements	Unknown Variables (N_v)	Memory	CPU Time	No. of Mesh Elements	Memory	CPU Time
1	61	2 k	5 k	200 MB	16 min	153 k	4.8 GB	106 min
2	21	0.5 k	1.3 k	15 MB	3 min	110 k	3.6 GB	63 min
3	41	1 k	2.7 k	60 MB	9 min	235 k	7.2 GB	125 min
4	101	17 k	50 k	190 MB*	194 min	450 k	9.0 GB	210 min

*In VIM, all the test cases except Test Case 4, have been solved using direct solver where allocation of memory size follows $8N_v^2$ relation. Due to the large problem domain, Test Case 4 is solved with an iterative solver, so the memory size is independent of the above relation.

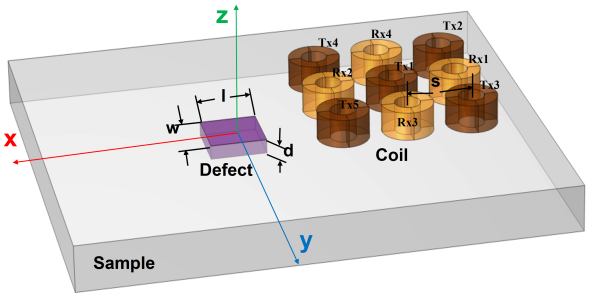

FIGURE 14. Schematic for a rectangular test piece with a rectangular defect and 9-element array probe (Tx-Rx-Tx coils) (Case 4).

probe domain requires dense meshing in VIM to account for all the current sources' interaction with the defective region. The corresponding discretized elements used to solve this problem are given in Table 8. The results obtained for the array probe are plotted in Fig. 15, which shows the magnitude difference between the two responses but in a similar shape. The discrepancy in results directs our assumption for Test Case 3 that the numerical calculations by two methods for multiple sources and receiver coils' responses do not comply with each other.

Experimental validation can be insightful for such test cases to find which methods provide better accuracy. However, for Test Case 1 with a single Tx-Rx probe, good agreement was observed by two methods, suggesting an alternative approach to investigate the root cause of the discrepancy. In this study, the impedance change was calculated by summing all the Rx coils' responses while simultaneously exciting all the driver coils. To identify the source of inconsistency in numerical calculations, multiple Tx-Rx combinations — such as Tx3-Rx4, Tx1-Rx1-Rx3, Tx2-Tx5-Rx2 — can be modeled while keeping the relative positions fixed to compare numerical results for each configuration. Although this approach is tedious, it can be perceived as an effective way to gain deeper insight into the two methods and could serve as a potential direction for future research.

3.5. Comparison of Computational Requirement by VIM and FEM

In Table 9, the computation costs are compared based on mesh elements/unknown variables and the execution time needed by the two methods. All the simulations were performed on a DELL Precision (Intel Xeon R) workstation with dual quad-core processors at 3.5 GHz and 16 GB of RAM. The CPU time required is provided as the total execution time for the full scan. The number of mesh elements or unknown variables indicates how large the memory is required by the numerical methods. The total unknown variables solved by VIM are approximately three times the number of mesh elements used for the discretization of the problem domain. It is noticeable that VIM needs less computational requirement than FEM since it solves integral equations over the defective region only. However, for Test Case 4, with multiple sources in a large array, the VIM and FEM demand similar computational resources. In such scenarios, FEM becomes more advantageous by providing user freedom of modeling customized probes. Despite the variations in magnitude for complicated probe geometry, the test cases presented in this research demonstrate the capabilities of the two numerical methods in modeling various EC inspection scenarios. It is evident from the results of this section that the proper utilization of numerical methods can be beneficial for EC inspection.

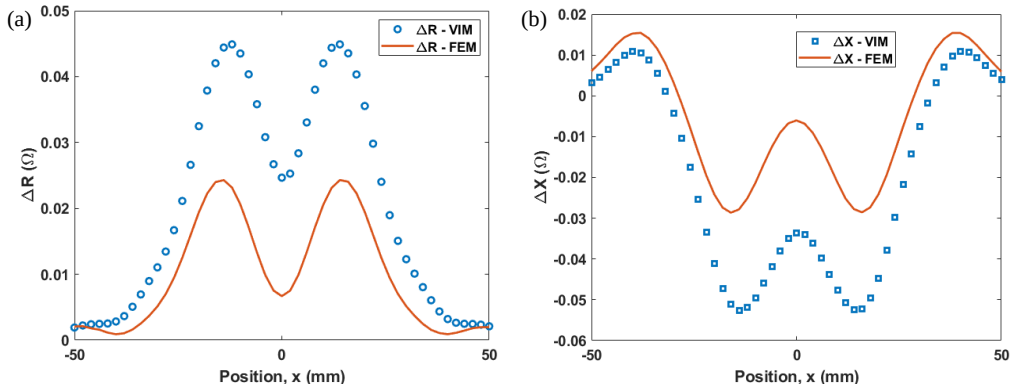

FIGURE 15. (a) Real part (ΔR) and (b) imaginary part (ΔX) of impedance change (ΔZ) as a function of the probe's center position (x) along the x-axis. The probe's center is the center of the Tx1 coil. The defect's center is oriented at the origin of the x-y plane.

4. CONCLUSIONS

This study has systematically compared two numerical methods — VIM and FEM for modeling eddy current NDE scenarios. The test cases explored in this study are a good fit for EC NDT applications, such as in power plants, industrial pipes, and metal plate manufacturing. The VIM method is more efficient for smaller problem domains, requiring less processing time than FEM, but is limited to simple geometries. In contrast, FEM, though time-consuming and computationally expensive, excels at meshing irregular surfaces and complex shapes, offering flexibility through partwise discretization. For large and critical probe models, both methods require nearly the same amount of computational time. VIM's efficiency and FEM's flexibility make them complementary methods, each suited to different aspects of eddy current NDE challenges. This study provides structured guidance for EC NDE modelers on utilizing numerical methods to optimize parameters, validate hypotheses, and generate MAPOD data before on-site implementation.

ACKNOWLEDGEMENT

This work was partly supported by a grant from the CNDE Membership Fund at ISU.

REFERENCES

[1] Kriezis, E. E., T. D. Tsiboukis, S. M. Panas, and J. A. Tegopoulos, "Eddy currents: Theory and applications," *Proceedings of the IEEE*, Vol. 80, No. 10, 1559–1589, 1992.

[2] Tavakoli, M. H., H. Karbaschi, and F. Samavat, "Computational modeling of induction heating process," *Progress In Electromagnetics Research Letters*, Vol. 11, 93–102, 2009.

[3] Bae, J.-S. and S.-Y. Kim, "Hot wire inspection using eddy current," in *IMTC 2001. Proceedings of the 18th IEEE Instrumentation and Measurement Technology Conference. Rediscovering Measurement in the Age of Informatics (Cat. No.01CH 37188)*, Vol. 2, 962–965, Budapest, Hungary, May 2001.

[4] Chebout, M., H. Azizi, and M. R. Mekideche, "A model assisted probability of detection approach for ECNDT of hidden defect in aircraft structures," *Progress In Electromagnetics Research Letters*, Vol. 95, 1–8, 2020.

[5] Vyroubal, D., "Impedance of the eddy-current displacement probe: The transformer model," *IEEE Transactions on Instrumentation and Measurement*, Vol. 53, No. 2, 384–391, 2004.

[6] Theodoulidis, T. P. and E. E. Kriezis, "Impedance evaluation of rectangular coils for eddy current testing of planar media," *NDT & E International*, Vol. 35, No. 6, 407–414, 2002.

[7] Zhou, H. T., K. Hou, H. L. Pan, J. J. Chen, and Q. M. Wang, "Study on the optimization of eddy current testing coil and the defect detection sensitivity," *Procedia Engineering*, Vol. 130, 1649–1657, 2015.

[8] Yang, X., Y. Feng, and S. Li, "Influence of measuring coil geometry on detection performance of eddy current sensor," in *IOP Conference Series: Materials Science and Engineering*, Vol. 452, No. 4, 042045, 2018.

[9] Mohseni, E., D. R. França, M. Viens, W. F. Xie, and B. Xu, "Finite element modelling of a reflection differential split-D eddy current probe scanning surface notches," *Journal of Nondestructive Evaluation*, Vol. 39, 1–14, 2020.

[10] Mooers, R. D., J. C. Aldrin, and J. S. Knopp, "Realistic split D differential probe model validation," in *AIP Conference Proceedings*, Vol. 1650, No. 1, 385–394, 2015.

[11] Das, N. K., P. Barat, S. Dey, and T. Jayakumar, "Design of miniature coil to generate uniform magnetic field," *Progress In Electromagnetics Research M*, Vol. 34, 99–105, 2013.

[12] Reverdy, F. and N. Dominguez, "NDT modeling tools applied to the aeronautic industry: Examples in CIVA," in *5th International Symposium on NDT in Aerospace*, Singapore, Nov. 2013.

[13] Maurice, L., V. Costan, E. Guillot, and P. Thomas, "Eddy current NDE performance demonstrations using simulation tools," in *AIP Conference Proceedings*, Vol. 1511, No. 1, 464–471, 2013.

[14] Mayos, M., O. Moreau, V. Costan, C. Gilles-Pascaud, C. Reboud, and F. Buvat, "A benchmark-based approach for the validation of eddy current simulation codes in support of nuclear power plants inspection," in *Electromagnetic Nondestructive Evaluation (XIII)*, 191–198, IOS Press, 2010.

[15] Chen, Z., N. Yusa, and K. Miya, "Some advances in numerical analysis techniques for quantitative electromagnetic nondestructive evaluation," *Nondestructive Testing and Evaluation*, Vol. 24, No. 1-2, 69–102, 2009.

[16] Biro, O., I. Bardi, K. Preis, W. Renhart, and K. R. Richter, "A finite element formulation for eddy current carrying ferromagnetic thin sheets," *IEEE Transactions on Magnetics*, Vol. 33, No. 2, 1173–1178, 1997.

[17] Xie, Y., F. Lu, and X. Ma, "Computation of eddy current problems by the finite volume method," in *ICEMS'2001. Proceedings of the Fifth International Conference on Electrical Machines and Systems (IEEE Cat. No.01EX501)*, Vol. 2, 1117–1120, Shenyang, China, 2001.

[18] Ratsakou, A., C. Reboud, A. Skarlatos, and D. Lesselier, "Fast models dedicated to simulation of eddy current thermography," in *Electromagnetic Non-Destructive Evaluation (XXI)*, 175–182, IOS Press, 2018.

[19] Sun, L. E. and W. C. Chew, "A novel formulation of the volume integral equation for electromagnetic scattering," *Waves in Random and Complex Media*, Vol. 19, No. 1, 162–180, 2009.

[20] Sabbagh, H. A., "A volume integral code for eddy-current nondestructive evaluation," *Applied Computational Electromagnetics Society Journal (ACES)*, Vol. 4, No. 1, 3–22, 1989.

[21] Sabbagh, H. A., R. K. Murphy, E. H. Sabbagh, J. C. Aldrin, and J. S. Knopp, *Computational Electromagnetics and Model-based Inversion*, 39–43, Springer-Verlag, New York, NY, 2013.

[22] Zeng, Z., L. Udpa, S. S. Udpa, and M. S. C. Chan, "Reduced magnetic vector potential formulation in the finite element analysis of eddy current nondestructive testing," *IEEE Transactions on Magnetics*, Vol. 45, No. 3, 964–967, 2009.

[23] Lu, M., A. Peyton, and W. Yin, "Acceleration of frequency sweeping in eddy-current computation," *IEEE Transactions on Magnetics*, Vol. 53, No. 7, 2017.

[24] Sultana, R., M. Lu, Y. Ji, J. C. Aldrin, and J. Song, "Evaluating eddy current simulation tools: A comparative analysis with benchmark cases," in *32nd ASNT Research Symposium*, Pittsburgh, PA, Jun. 2024.

[25] Victor Technologies, L., VIC-3D eddy-current NDE software, [Online]. Available: http://www.sabbagh.com/products.html, 2013.

[26] COMSOL, I. AC/DC module user's guide, version 6.0, [Online]. Available: https://doc.comsol.com.

[27] Team workshop problem 15 rectangular slot in a thick plate: A problem in nondestructive evaluation, [Online]. Available: https://www.compumag.org/jsite/images/stories/TEAM/problem15.pdf.

[28] Xie, H., Y. Ji, and J. Bowler, "Eddy current pancake coil measurements on a longitudinal through-wall notch in an inconel tube," [Online]. Available: https://www.wfndec.org/benchmarkproblems, 2012.

[29] Foucher, F., L. Maurice, T. Sollier, C. Reboud, D. François, A. Trillon, and P. Thomas, "Evaluating eddy current simulation tools: A comparative analysis with benchmark cases," in *11th European Conference on Nondestructive Testing (ECNDT)*, Prague, Czech Republic, Oct. 2014.

[30] CST studio suite, [Online]. Available: https://www.3ds.com/products/simulia/cst-studio-suite, 2024.

[31] Aoukili, A. and A. Khamlichi, "Modeling an eddy-current probe for damage detection of surface cracks in metallic parts," *Procedia Technology*, Vol. 22, 527–534, 2016.